CRYSTAL GROWTH & DESIGN

pubs.acs.org/crystal

Article

Solvothermal Crystallization Kinetics and Control of Crystal Size Distribution of MOF-808 in a Continuous Flow Reactor

Sujay D. Bagi, Allan S. Myerson, and Yuriy Román-Leshkov*

Cite This: *Cryst. Growth Des.* 2021, 21, 6529−6536

Read Online

ACCESS | Metrics & More | Article Recommendations | Supporting Information

ABSTRACT: A fundamental understanding of the crystallization pathways for metal−organic frameworks (MOFs) allows for exploring the untapped combinatorial space of the organic and inorganic building units, creating possibilities to synthesize highly crystalline frameworks with desired physicochemical properties. In this work, we employ a continuous flow reactor to elucidate the kinetics of crystallization for the Zr-based MOF-808 using time-resolved powder X-ray diffraction measurements. Specifically, we fit the crystallization curves obtained experimentally using the Gualtieri model to determine the rate constants for nucleation (k_N) and growth (k_G) for different linker concentrations and temperatures. Higher linker concentrations reduce the competitive coordination of the formate ligand (growth modulator) with the secondary building unit, resulting in higher nucleation and growth rates. The activation energies obtained from Arrhenius plots for nucleation ($E_a(N)$) and growth ($E_a(G)$) are 64.7 ± 4 and 59.2 ± 5 kJ mol^{-1}, respectively. At constant residence time, temperature, and composition, higher flow velocities increase the advective transport of precursor species to nucleation sites in the slugs resulting in increased crystal growth rates and thus higher average crystal sizes. Variation in the total flow rate from 0.334 to 1.067 mL/min increased the average crystal sizes from ∼105 ± 22 to ∼180 ± 19 nm, with other parameters held constant. We demonstrate that performing crystallization in the flow reactor provides a unique opportunity to tailor MOF crystal sizes. By strictly controlling the temperature, residence time, and mixing parameters, our results showcase the advantages of flow systems for performing rigorous crystallization and structural evolution studies that can be applied for the synthesis of other MOFs with tailored physicochemical properties.

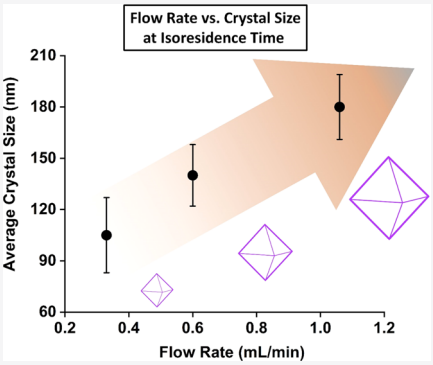

INTRODUCTION

Metal−organic frameworks (MOFs) are coordination complexes consisting of organic linkers and inorganic polynuclear clusters that form two- and three-dimensional structures.[1] The numerous ways in which the organic and inorganic units can be combined have led to the discovery of thousands of new frameworks with unique properties that can be targeted for use in industrially attractive applications.[2] Zr-based MOFs are particularly important due to their chemical stability, as well as amenability to postsynthetic modification (PSM).[3] MOF-808, first reported by Furukawa et al.,[4] is formed from the assembly of a $Zr_6(\mu_3\text{-}O)_4(\mu_3\text{-}OH)_4(CO_2)_{12}$ (referred to as Zr_6-cluster) inorganic secondary building unit and benzene-1,3,5-tricarboxylic acid (H_3BTC) organic linkers.[3] The resulting structure features large cavities (diameter of 18.4 Å) and Brunauer−Emmett−Teller (BET) surface areas of ∼2000 m^2·g^{-1}. Monocarboxylic ligands, such as formate, acetate, and propionate, are employed as crystal growth modulators in MOF-808 synthesis to regulate crystal size and increase the crystallinity of the framework.[5,6] Although MOF-808 has been demonstrated for use in a number of industrially relevant applications ranging from catalysis[7−9] and water harvesting[10] to heavy metal capture[11] and arsenic removal,[12] details pertaining to the kinetics of crystallization or the control of crystal size distributions (CSDs) have not been reported. A thorough understanding of the self-assembly of MOF building units along with the reaction pathways to achieve precise control over the crystallization process would help in optimizing MOF synthesis to yield the desired crystallinity and provide important parameters for synthesis scale-up.

Tailored physicochemical properties of Zr-MOFs can be achieved by coordination modulation, using organic ligands with a similar chemical functionality as the linker to compete for coordination sites at the SBU.[6,13] In the presence of a modulator, nucleation and crystal growth proceed at a reduced rate. The crystallization process requires an equilibrium between crystal formation and dissolution to allow for sufficient reorganization and defect reparation during the early stages of crystal growth.[3,14] Accordingly, evaluating the amount of modulator, linker concentration, residence time, and temperature in the extent of crystallization is imperative to achieve the desired CSD, crystallinity, and product yields.

Received: August 23, 2021
Revised: September 30, 2021
Published: October 20, 2021

https://doi.org/10.1021/acs.cgd.1c00968
Cryst. Growth Des. 2021, 21, 6529−6536

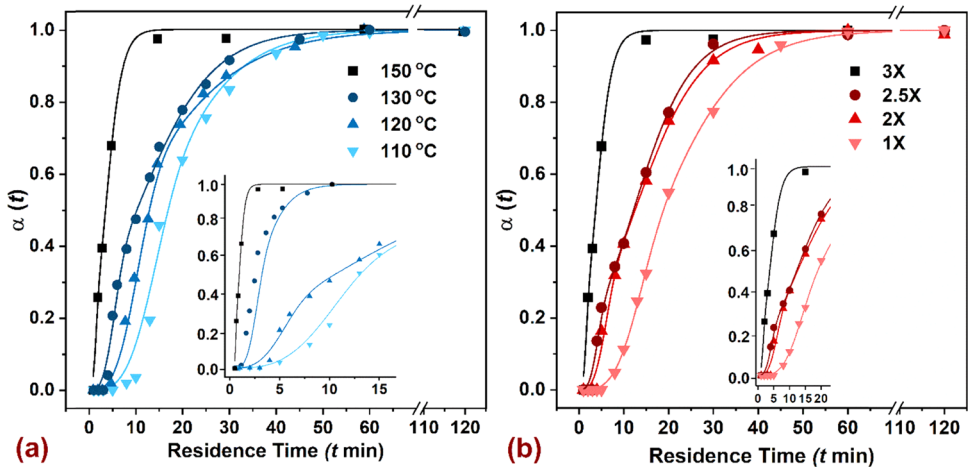

Figure 1. Extent of crystallization $\alpha(t)$ plotted against time t (closed symbols) and the corresponding Gualtieri fitting (solid curves) to investigate the (a) influence of reaction temperature (110−150 °C) at a 3× linker concentration and (b) influence of linker concentration (1× to 3×) at 150 °C on the rates of crystallization. The inset images show fitted data for residence times below 15 min.

The use of microfluidic flow reactors offers the ability to explore a wide range of synthetic parameters in a short amount of time with minimal consumption of reagents, making them ideal to extract kinetic information.[15−17] Unlike batch reactors used for in situ diffraction experiments that intrinsically operate in a transient mode, flow reactors allow studies of the crystallization process at a steady state with precise control over temperature and residence time, thereby enabling time-resolved crystallization studies for any MOF of interest. Here, we use a biphasic liquid−liquid slug flow in our reactor to perform continuous microbatch MOF crystallization studies. In situ diffraction techniques such as energy-dispersive X-ray diffraction (EDXRD)[18−20] and small-angle X-ray scattering (SAXS)[21,22] are commonly used to study kinetics of MOF crystallization. They entail the use of a heating apparatus for the reaction mixture, which is loaded into a vial (analogous to a batch reactor) and placed in the X-ray beam path to monitor the evolution of diffraction peaks as a function of time. Although in situ diffraction measurements allow for a better temporal resolution compared to individual samples synthesized at various residence times to study the evolution of crystallinity, it is difficult to study the influence of parameters such as mixing of reagents, shear rates, and flow-induced molecular transport on nucleation and growth kinetics in batch systems. Here, we report the use of flow reactors to elucidate the kinetics of crystallization for MOF-808. The time-resolved crystallization studies were performed by synthesizing MOF samples at desired residence times and temperatures, using powder X-ray diffraction (PXRD) to monitor the extent of crystallization by integrating the area under prominent Bragg diffraction peaks. We obtained rate constants of nucleation and growth as a function of temperature and linker concentration by implementing nonlinear fitting of the corresponding crystallization curves to the Gualtieri model. The rate constants obtained at different temperatures were used to calculate activation energies for nucleation and growth using Arrhenius plots. Finally, we report that the flow rate and slug volume can be used as orthogonal variables for tuning the crystal size distribution (CSD) of MOFs with narrow polydispersity ranges. Our work highlights the advantages of flow systems to obtain intrinsic parameters governing the crystallization of MOFs, as well as of the use of reactor operational parameters unique to flow systems to generate MOFs with tailored CSDs.

RESULTS AND DISCUSSION

A continuous flow reactor operating in a biphasic liquid−liquid slug-flow regime offers the ability to precisely control residence time.[23] In our flow reactor, silicone oil is used as an immiscible continuous phase because it preferentially wets the PTFE reactor tubing and encapsulates the slugs (μL droplets) of the dispersed phase containing the MOF precursors.[24] Importantly, the miniaturization of the reaction system reduces diffusion lengths, aids in rapid mixing of reagents, and enables fast heat and mass transport, along with tight control of residence times (order of milliseconds), all critical elements to monitor nucleation and crystallization events with high fidelity. As the precursor slugs traverse the heated reaction zone, viable nucleation sites emerge from short-range crystalline order, followed by grain growth, and culminating in MOF crystals. The schematic for the flow reactor is illustrated in Figure S1 of the Supporting Information, and details pertaining to reactor components and operations are provided in our previous work.[24] To collect the large number of samples to perform this time-resolved crystallization study, we developed a rapid sampler module connected to the outlet of the flow reactor (Figure S2), which facilitates easy sampling by quenching the reactions at desired residence times. MOF solids collected at the reactor outlet are filtered and washed twice with *N*,*N*-dimethylformamide (DMF) followed by acetone, before undergoing characterization with powder X-ray diffraction (PXRD). Figure S3 shows the PXRD pattern along with Miller indices of the prominent peaks for MOF-808. The evolution of crystallinity as a function of time is monitored using the extent of crystallization ($\alpha(t)$), which is the ratio of the integrated intensity $I(t)$ of a prominent peak at any residence time t to the maximum intensity I_{max} of the peak obtained after complete crystallization (eq 1). For MOF-808, the (400) reflection was chosen to calculate $\alpha(t)$ as there are no overlapping peaks or any pre- or postedge features that could increase the error when calculating the area under the curve. The crystallization curves ($\alpha(t)$ *vs* t) obtained at 110 and 150 °C are shown in Figure S4. After a short induction time, long-range crystalline order could be detected and the reflections from the (400)

https://doi.org/10.1021/acs.cgd.1c00968
Cryst. Growth Des. 2021, 21, 6529−6536

Table 1. Kinetic Parameters Obtained by Fitting the Crystallization Curves Obtained at Four Different Temperatures Using the Gualtieri Model[a]

temperature (°C)	a (min)	b (min)	n	k_G (min^{-1})	k_N (min^{-1})	R^2
110	23.87	19.44	3	0.070 ± 0.013	0.041 ± 0.006	0.991
120	17.29	12.43	3	0.089 ± 0.003	0.057 ± 0.007	0.998
130	9.26	6.81	3	0.163 ± 0.011	0.107 ± 0.005	0.996
150	3.69	1.78	3	0.382 ± 0.038	0.271 ± 0.011	0.998

[a]The linker concentration for all conditions was 3×.

Table 2. Kinetic Parameters Obtained by Fitting the Crystallization Curves Obtained at Four Different Linker Concentrations Using the Gualtieri Model[a]

linker concentration	a (min)	b (min)	n	k_G (min^{-1})	k_N (min^{-1})	R^2
1×	18.07	9.2	3	0.078 ± 0.002	0.055 ± 0.004	0.999
2×	12.49	7.32	3	0.167 ± 0.018	0.080 ± 0.002	0.996
2.5×	12.16	6.34	3	0.238 ± 0.021	0.082 ± 0.004	0.996
3×	3.69	1.78	3	0.382 ± 0.038	0.271 ± 0.015	0.998

[a]The reaction temperature for all conditions was held at 150 °C.

plane gained intensity until they reached their respective maxima beyond which there was no change in $I(t)$. Since the crystallization curves obtained from Bragg reflections of the (400) and (331) planes are superimposable, the presence of the preferred orientation of crystals influencing the integrated peak area can be excluded (Figure S4)[25]

$$\alpha(t) = \frac{I(t)}{I_{max}} \quad (1)$$

The crystallization behavior of MOFs strongly depends on reaction conditions such as temperature, residence time, concentration of reactants, and the type of solvents employed.[26,27] To gain insights into the solvothermal crystallization of MOF-808, we assessed the role of temperature and linker concentration in the reaction mixture. The crystallization curves obtained from MOF syntheses at four different temperatures (110, 120, 130, and 150 °C) in the continuous flow reactor are shown in Figure 1a, while the curves from four different linker concentrations (1×, 2×, 2.5×, and 3×) are shown in Figure 1b. The linker concentration of 1× in the reaction mixture corresponds to 0.33 mmol of benzene-1,3,5-tricarboxylic acid (H_3BTC) based on the synthesis procedure reported by Jiang et al.[8] The composition of 2× corresponds to a 2-fold increase of linker concentration in the reaction mixture with other parameters held constant; additional details pertaining to the reaction mixture composition are provided in Table S2 and Part 2 of the SI. The linker concentration used for all of the crystallization curves in Figure 1a was 3×, while a reaction temperature of 150 °C was used for all conditions explored in Figure 1b. The kinetic evaluation of the crystallization curves was performed by fitting the data (closed symbols) in Figure 1 with the Gualtieri model, which was originally derived for the heterogeneous crystallization of a solid from a liquid by Gualtieri.[28] The Gualtieri model (eq 2) is well suited for evaluating solution-mediated transformation reactions and allows differentiating nucleation and crystal growth by treating them as individual processes compared to the commonly used Avrami−Erofeev (AE) model, which was developed for solid-state processes.[20,29] The Gualtieri expression relates the extent of crystallization $\alpha(t)$ as a function of residence time t, the rate constant of growth k_G, the fitting parameters a and b, along with the dimensionality of crystal growth n, which was set to 3 for MOF-808 as it crystallizes in the $Fd\bar{3}m$ space group (cubic crystal system).[8,26,30] The fitting parameters a and b are used to calculate the probability of nucleation P_N, which is described later in the study. The rate constant for nucleation k_N is calculated from the fitting parameter ($k_N = 1/a$). The induction time (t_0) defined as the period during which no crystalline products are observed was shorter for synthesis at higher temperatures; for instance, t_0 is 5 min at 110 °C, which reduces to 1 min at 150 °C. Furthermore, the residence times for complete crystallization t_f at $\alpha(t) = 1$ were shorter at higher temperatures (5 min at 150 °C, increasing to ∼60 min at 110 °C). Table S3 summarizes t_o and t_f for all reaction conditions explored. The kinetic parameters obtained by fitting the Gualtieri model to the crystallization curves obtained at different temperatures along with R^2 values are summarized in Table 1. The values for both k_G and k_N increase with temperature as expected for a reactive-crystallization process.[31] At each temperature, $k_N < k_G$ implying that the nucleation is slower than crystal growth. All k values increase by an order of magnitude as the temperature increases from 110 to 150 °C.

Similarly, the reactions carried out by varying linker concentrations (Figure 1b) provide insight into the coordination modulation mechanism for MOF-808. Table 2 summarizes the kinetic parameters obtained for reaction conditions with varying linker concentrations at 150 °C. A higher linker concentration in the reaction mixture enhances the linker coordination with the SBU by reducing the competitive coordination of the formate ligand, leading to an increase in the reaction rates. For a 3× linker concentration, the molar ratio of formic acid to Zr metal (acid/metal) is 176, while a 1× linker concentration results in a molar ratio of 528.3, indicating higher competition by the formate ligand for coordination with the SBU (Table S2). Lower reaction rates with a higher acid/metal ratio translate to lower rates for the self-assembly process of MOFs.[32] The induction time t_0 is 8 min for 1× concentration, which decreases to 1 min for the 3× condition. The residence times for complete crystallization were shorter at higher concentrations (5 min at 3×, 40 min at 2.5×, 45 min at 2×, and 60 min at 1×). The values for k_G and k_N increase with the linker concentration, which is in line with the concept of coordination modulation.[3,13] Larger amounts of modulator (formic acid) in the reaction mixture lead to slower nucleation rates, k_N, resulting in fewer nucleation sites that grow at a

https://doi.org/10.1021/acs.cgd.1c00968
Cryst. Growth Des. 2021, 21, 6529−6536

decreased growth rate k_G for all reaction conditions, $k_N < k_G$, implying the nucleation step to be rate-limiting. The k values for both nucleation and growth increase by an order of magnitude as the linker concentration is increased from 1× to 3×. We also use the AE expression (eq S1 and Section 3 in SI) as a second model to fit the crystallization curves. The curve fitting for the extent of crystallization $\alpha(t)$ is shown in Figures S5 and S6 for different temperatures and linker concentrations, respectively. The kinetic parameters, such as the overall rate constant k and the Avrami exponent n_{AE}, are tabulated in Tables S4 and S5. Values for n_{AE} in the range of 0.6−1 are characteristic of a first-order reaction mechanism and suggest that crystallization is controlled by the formation of nucleation sites.[20,29,33] The k values obtained from the AE model are of the same order of magnitude compared to those of the Gualtieri model and increase by more than 5-fold with temperature (110−150 °C) and 8-fold with the linker concentration (1× to 3×).

$$\alpha(t) = \frac{1}{1 + e^{-(t-a)/b}}[1 - e^{-(k_G \cdot t)^n}] \quad (2)$$

The crystallization process of MOFs proceeds via two steps: nucleation of discrete particles followed by crystal growth, which typically results in an S-shaped curve.[34] The nucleation sites in the reaction mixture are not directly visible in the diffraction experiments and are estimated by the Gualtieri model by defining the probability of nucleation P_N (eq 3). The expression for P_N has a Gaussian distribution of probabilities for the total number of nuclei N present at time t while the fitting parameter a gives the position of the top of the Gaussian peak (maximum rate of nucleation), and the parameter b is the variance of the peak describing the distribution of the probability with time.[20,28] The plot of P_N versus t (blue curve) for the crystallization curve obtained at 130 °C and 3× linker concentration is shown in Figure 2. Nucleation can be seen to extend well into the crystal growth regime and follows a Gaussian distribution to estimate the presence of viable nucleation sites at time t. The probability of nucleation for different temperatures and linker concentrations is shown in Figures S7 and S8, respectively. An increase in temperature leads to a faster nucleation rate with an earlier maximum as indicated by the values of fitting parameter a, while P_N becomes negligible toward the end of the crystal growth regime ($\alpha(t) > 0.9$). The maximum rate of nucleation occurs at ∼24 min at 110 °C, which reduces to ∼4 min at 150 °C. Similarly, an increase in the linker concentration also reduces the time at which the maximum nucleation rate occurs, ∼18 min at 1× reducing to ∼4 min at 3× concentration. Since nucleation rates are strongly dependent on the level of supersaturation of the reaction mixture, an increase in the linker concentration achieves higher nucleation rates at lower residence times.[35]

$$P_N = \frac{dN}{dt} = e^{-((t-a)^2/2b^2)} \quad (3)$$

The rate constants for nucleation k_N and growth k_G obtained by fitting the crystallization curves with the Gualtieri model allow for calculating the corresponding activation energies $E_A(N)$ and $E_A(G)$ for nucleation and growth, respectively. The activation energies are calculated by linear fitting of the Arrhenius expressions (eqs 4 and 5) in $\ln k$ *vs* $1/T$ plots as shown in Figure 3 along with the appropriate error bars. The

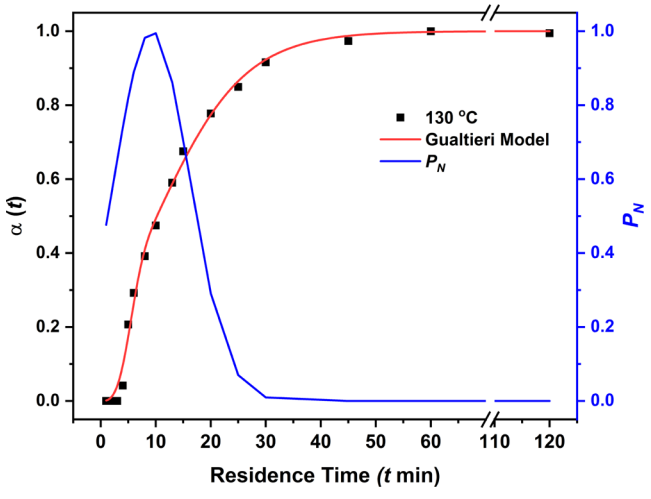

Figure 2. Extent of crystallization $\alpha(t)$ plotted against time t (closed symbol), the corresponding Gualtieri fitting (red curve), and the probability of nucleation P_N (blue curve). The crystallization curve was obtained at 130 °C with a linker concentration of 3×.

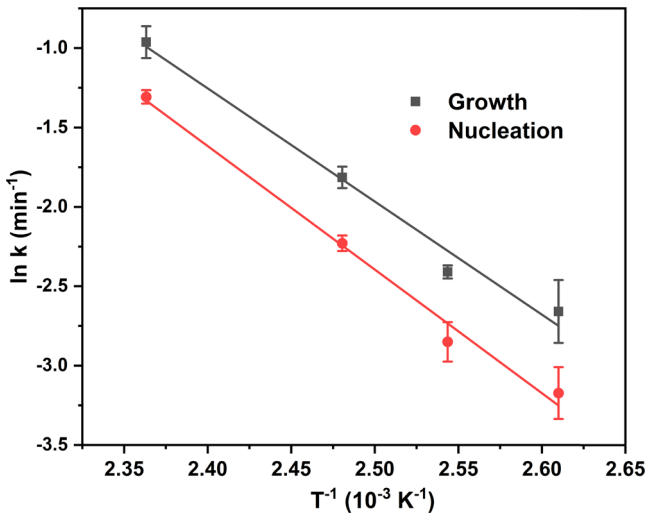

Figure 3. Arrhenius plots for the temperature-dependent rate constants of nucleation (red circles) and growth (gray squares) at a 3× linker concentration obtained from the evaluation of the Gualtieri model.

Arrhenius expression correlates the rate constant k with the pre-exponential factor A, reaction temperature T, the universal gas constant R, and the activation energy E_A. The values for $E_A(N)$ and $E_A(G)$ determined by the slopes of the linear regression are 64.7 ± 4 and 59.2 ± 5 kJ·mol^{-1}, respectively (Table 3). We calculate $E_A(N)$ and $E_A(G)$ only for the case of 3× linker concentration. The rate enhancement in crystallization is likely not due to a supersaturation effect and instead supports the hypothesis of inherent changes in the transport/kinetics. The values for both activation energies do not deviate much from each other and are fairly close to the values reported by Zahn et al.[13] for MOF-801 (71 ± 3 kJ·mol^{-1} for $E_A(N)$ and 66 ± 6 kJ·mol^{-1} $E_A(G)$). They hypothesized that both energies reflect the same chemical reaction that is the exchange of modulator ligand on the Zr_6-cluster (SBU), which would not be influenced by the size of the growing entity—either a small nucleation site or a larger crystal. MOF-801 also

https://doi.org/10.1021/acs.cgd.1c00968
Cryst. Growth Des. 2021, 21, 6529−6536

Table 3. Activation Energies for Nucleation and Growth Obtained from Arrhenius Plots for k_N and k_G[a]

temperature (°C)	k_N (min^{-1})	k_G (min^{-1})	$E_A(N)$ (kJ·mol^{-1})	$E_A(G)$ (kJ·mol^{-1})	R^2
110	0.041	0.070	64.7 ± 4	59.2 ± 5	0.991 (nucleation)
120	0.057	0.089			
130	0.107	0.163			0.984 (growth)
150	0.271	0.382			

[a]The linker concentration for all conditions was 3×.

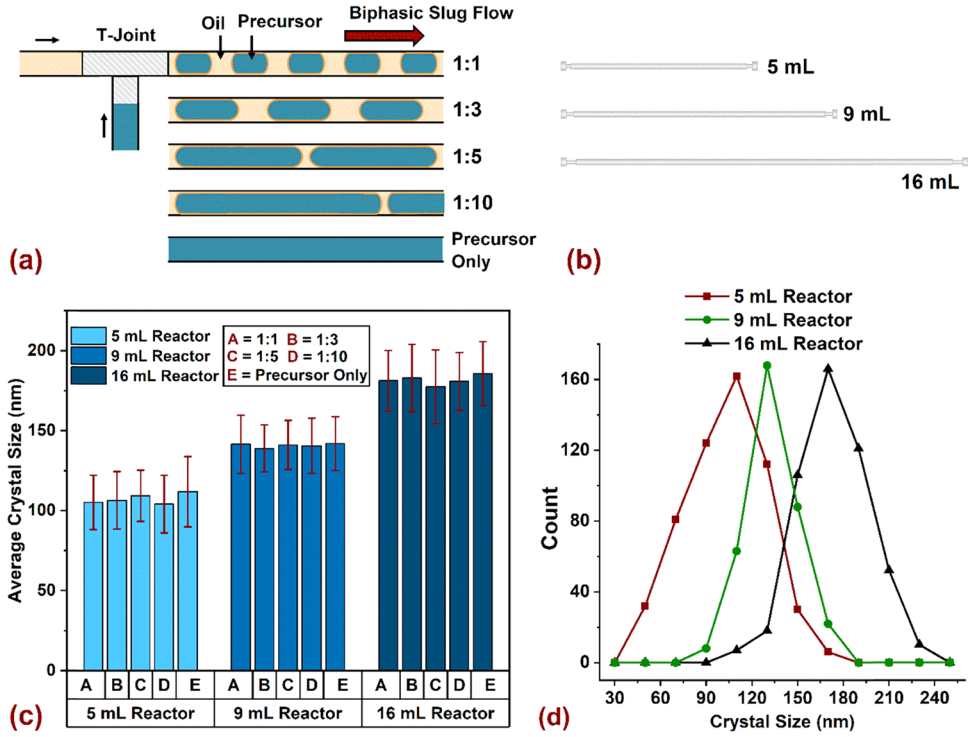

Figure 4. (a) Schematic representation of the biphasic liquid−liquid slug flow at different volumetric ratios of silicone oil (continuous phase) and the precursor mixture (dispersed phase). (b) Illustration of three different reactor configurations used in the study with the same tube ID (1/16 in. or 1.58 mm). (c) Average crystal sizes obtained from 5, 9, and 16 mL reactors along with error bars representing 1 standard deviation for all volumetric ratios of "oil/precursor". (d) CSD as a function of reactor volume for the single-phase flow condition (precursor only).

known as the Zr-fumarate MOF uses similar reagents in the reaction mixture (Zr salt, *N*,*N*-DMF, formic acid, and fumaric acid as the linker) compared to MOF-808. The activation energy calculated from the AE model using the overall rate constant k was 57.3 ± 4 kJ·mol^{-1}, which is in close agreement with the values obtained from the Gualtieri model (Figure S9). In general, the calculated activation energies for MOF-808 are of the same order of magnitude compared to the values reported for other MOFs such as HKUST-1,[18] ZIF-8,[36] and UiO-66[19] (Table S6)

$$k_N = A\ e^{-(E_a(N)/RT)} \rightarrow \ln k_N = \ln A - \frac{E_a(N)}{RT} \quad (4)$$

$$k_G = A\ e^{-(E_a(G)/RT)} \rightarrow \ln k_G = \ln A - \frac{E_a(G)}{RT} \quad (5)$$

Slug-flow crystallizers have recently been used to perform cooling crystallization,[37−39] reactive crystallization,[40−42] and antisolvent crystallization[43,44] as they provide many degrees of freedom for controlling CSD and morphology with a high degree of reproducibility while also providing easier scale-up and higher process productivity compared to batch. Achieving reproducible and a narrow CSD is desirable for manufacturing crystalline materials with desired physicochemical characteristics, which simplifies the downstream processing steps.[45] In this study, we use our flow reactor to examine the effects of flow rate and volume of the MOF precursor (reaction mixture) contained in the slugs on the CSD of MOF-808. The reactor tube ID was fixed to 1/16 in. (1.58 mm) as it was best suited to achieve optimal mixing in the slugs without lowering the throughput. The use of static mixers is not viable for our system as it would disrupt the slug-flow pattern. We investigated five different biphasic slug-flow configurations achieved by varying the ratio of volumetric flow rates for silicone oil (continuous phase) and the precursor (dispersed phase). All of the conditions explored had a residence time of 15 min at a temperature of 150 °C and a 3× linker concentration in the reaction mixture, which ensured completion of the crystallization process $\alpha(t) = 1$ (Figure 1a and Table S3). Figure 4a provides a schematic for these configurations, wherein a biphasic slug flow in a 16 mL reactor for a 1:1 "oil/precursor" was achieved with a flow rate of 0.53 mL/min for both the phases, while a 1:10 configuration was achieved with a flow rate of 0.097 mL/min for oil and 0.97 mL/min for the precursor phase (Table S7). The "precursor-only" condition was used to study the effects of mixing patterns encountered in a single-phase flow in a PFR compared to the

https://doi.org/10.1021/acs.cgd.1c00968
Cryst. Growth Des. 2021, 21, 6529−6536

biphasic slug-flow regime. There was no droplet coalescence observed across these biphasic slug-flow configurations. Figure S10 shows reproducible droplets (white slugs) containing crystalline MOF particles as the dispersed phase and the silicone oil (transparent slugs) as the continuous phase, at the reactor outlet for a 1:1 oil/precursor volumetric ratio and reaction conditions of 150 °C and a 15 min residence time. We also studied the effects of the flow rate on CSD by varying the length of the reactor tubing with the same inner diameter (1/16 in.) while maintaining a constant residence time of 15 min (Figure 4b and Table S6). Microcrystalline MOF-808 samples synthesized from all reactor configurations were imaged using a high-resolution transmission electron microscope (TEM), and the corresponding crystal sizes were measured using the ImageJ software program based on a procedure reported by Hirschle et al.[46] (Figures S11−S13). Average crystal sizes shown in Figure 4c are obtained from measurements of ∼500 nanoparticles for every biphasic slug-flow configuration from three different reactors, while the error bars correspond to 1 standard deviation. Interestingly, the average crystal sizes had a positive correlation with an increase in the total flow rate while maintaining a residence time of 15 min for all conditions. For instance, a total flow rate of 0.334 mL/min in a 5 mL reactor resulted in average crystal sizes of ∼105 ± 22 nm, while a total flow rate of 1.067 mL/min in a 16 mL reactor resulted in crystal sizes of ∼180 ± 19 nm. However, there was no change in CSD with variations of biphasic slug-flow configurations pertaining to the volumetric flow ratios of "oil/precursor" across all reactors. Similar observations were made for the single-phase flow condition (precursor only), which also resulted in an increase in average crystal sizes with higher flow rates. Figure 4d shows CSD trends for the precursor-only condition, with the mean sizes being ∼105 nm for the 5 mL reactor, ∼140 nm for the 9 mL reactor, and ∼180 nm for the 16 mL reactor. The CSD trends for all of the biphasic slug-flow configurations are provided in Figures S11−S13. To the best of our knowledge, this is the first report of using flow rates and slug volume to tune the crystal sizes of MOFs while achieving a narrow size distribution.

The variation in CSD as a function of total flow rate can be explained by considering the mixing effects in the precursor slugs moving through a millifluidic channel. Each precursor slug is a well-mixed microbatch reactor where the mixing of reagents occurs over the order of milliseconds and is accomplished by chaotic advection, which originates from recirculating flow patterns inside the slug.[47] Song et al.[48] provided a scaling argument for estimating the characteristic mixing time t_{mix} as a function of the dimensionless Péclet number Pe (eqs S3 and S4 and Section 4 of the SI). An increase in the flow rate results in a higher rate of advective transport for reagents leading to a larger Pe and a smaller t_{mix} (Table S8). For instance, to achieve a residence time of 15 min in a 16 mL reactor, the total flow rate of 1.067 mL/min results in a Pe of 14 180. Similarly, the Pe numbers in 9 and 5 mL reactors are 7166 and 4440, respectively. Higher Pe values translate to the enhanced flow-mediated transport of precursor species to the nucleation sites in the precursor slugs, which accelerates the crystal growth rates leading to a faster consumption of reagents in the slug.[49] Since the reaction mixture composition for all conditions explored remained constant (3× linker concentration), the nucleation rate J, which strongly depends on the level of supersaturation S, remains the same (eq S5). As the precursor slugs enter the heated reaction zone of the flow reactor, the nucleation rate would be similar across all reactor configurations; however, higher flow rates to achieve the same residence time of 15 min leads to a larger Pe and consequently higher crystal growth rates. Since the reaction mixture is compartmentalized in individual slugs, higher crystal growth rates result in a simultaneous reduction in the nucleation rate owing to lower levels of supersaturation upon faster consumption of reagents. This phenomenon can be used to elucidate the CSD trends evident in our flow reactor as a function of total flow rates and offers a simpler control for manipulating the crystal sizes without requiring complicated experimental setup for supersaturation control, nonmonotonic temperature profiles among others.

CONCLUSIONS

In this work, we investigated the kinetics of crystallization for Zr-based MOF-808 using a continuous flow reactor. The rate constants for nucleation k_N and growth k_G were obtained by nonlinear fitting of crystallization curves with the Gualtieri model, which is well suited for evaluating solution-mediated transformation reactions. For all reaction conditions explored, $k_N < k_G$ and the values for both k_N and k_G increased by more than 5-fold with the temperature (110−150 °C) and linker concentration in the reaction mixture (1× to 3×). Activation energies for nucleation $E_A(N)$ and growth $E_A(G)$ determined from Arrhenius plots were 64.7 ± 4 and 59.2 ± 5 kJ·mol^{-1}, respectively, while the activation energy calculated from the AE model using the overall rate constant k was 57.3 ± 4 kJ·mol^{-1}, which is in close agreement with the Gualtieri model. Our study provides the first account for the use of flow rates in the reactor as a simpler tool for tuning the crystal sizes of MOFs with a narrow distribution. Average crystal sizes of ∼105 ± 22 nm were achieved with a total flow rate of 0.334 mL/min (5 mL reactor), ∼140 ± 18 nm with a total flow rate of 0.6 mL/min (9 mL reactor), and ∼180 ± 19 nm with a total flow rate of 1.067 mL/min (16 mL reactor). For a constant residence time across all reactor configurations, an increase in the flow rate enhances the flow-mediated transport of precursor species to the nucleation sites, thereby accelerating the crystal growth, accompanied by a simultaneous reduction in the nucleation rate due to faster consumption of reagents—the phenomenon responsible for CSD trends seen in our flow reactor. The results presented in this work allow for a better understanding of nucleation and crystal growth kinetics of self-assembled porous frameworks along with additional degrees of control offered by flow reactors to synthesize MOFs with the desired physicochemical properties for real-world applications.

ASSOCIATED CONTENT

Supporting Information

The Supporting Information is available free of charge at https://pubs.acs.org/doi/10.1021/acs.cgd.1c00968.

Description of flow synthesis platform, materials and experimental methods, reactor operational parameters, kinetic data evaluation for Avrami−Erofeev models, and CSD obtained for three different reactor configurations are provided (PDF)

https://doi.org/10.1021/acs.cgd.1c00968
Cryst. Growth Des. 2021, 21, 6529−6536

AUTHOR INFORMATION

Corresponding Author

Yuriy Román-Leshkov − *Department of Chemical Engineering, Massachusetts Institute of Technology, Cambridge, Massachusetts 02139, United States*; Phone: 617 253 7090; Email: yroman@mit.edu; Fax: 617 253 7090

Authors

Sujay D. Bagi − *Department of Mechanical Engineering, Massachusetts Institute of Technology, Cambridge, Massachusetts 02139, United States; Department of Chemical Engineering, Massachusetts Institute of Technology, Cambridge, Massachusetts 02139, United States*; orcid.org/0000-0001-7028-190X

Allan S. Myerson − *Department of Chemical Engineering, Massachusetts Institute of Technology, Cambridge, Massachusetts 02139, United States*; orcid.org/0000-0002-7468-8093

Complete contact information is available at: https://pubs.acs.org/10.1021/acs.cgd.1c00968

Notes

The authors declare no competing financial interest.

ACKNOWLEDGMENTS

S.B., A.S.M., and Y.R.-L. would like to thank the U.S. Department of Energy, Office of Basic Energy Sciences under Award DE-SC0016214 for support. The authors would also like to thank Dr. Yong Zhang for technical assistance with TEM and Dr. Shuai Yuan for fruitful discussions on the crystallization kinetics of Zr-based MOFs.

REFERENCES

(1) Rowsell, J. L. C.; Yaghi, O. M. Metal-organic frameworks: a new class of porous materials. *Microporous Mesoporous Mater.* **2004**, *73*, 3−14.

(2) Furukawa, H.; Cordova, K. E.; O'Keeffe, M.; Yaghi, O. M. The Chemistry and Applications of Metal-Organic Frameworks. *Science* **2013**, *341*, 673.

(3) Yuan, S.; Feng, L.; Wang, K.; Pang, J.; Bosch, M.; Lollar, C.; Sun, Y.; Qin, J.; Yang, X.; Zhang, P.; Wang, Q.; Zou, L.; Zhang, Y.; Zhang, L.; Fang, Y.; Li, J.; Zhou, H.-C. Stable Metal-Organic Frameworks: Design, Synthesis, and Applications. *Adv. Mater.* **2018**, *30*, No. 1704303.

(4) Furukawa, H.; Gandara, F.; Zhang, Y. B.; Jiang, J. C.; Queen, W. L.; Hudson, M. R.; Yaghi, O. M. Water Adsorption in Porous Metal-Organic Frameworks and Related Materials. *J. Am. Chem. Soc.* **2014**, *136*, 4369−4381.

(5) Liang, W.; Chevreau, H.; Ragon, F.; Southon, P. D.; Peterson, V. K.; D'Alessandro, D. M. Tuning pore size in a zirconium−tricarboxylate metal−organic framework. *CrystEngComm.* **2014**, *16*, 6530−6533.

(6) Schaate, A.; Roy, P.; Godt, A.; Lippke, J.; Waltz, F.; Wiebcke, M.; Behrens, P. Modulated Synthesis of Zr-Based Metal-Organic Frameworks: From Nano to Single Crystals. *Chem. − Eur. J.* **2011**, *17*, 6643−6651.

(7) Baek, J.; Rungtaweevoranit, B.; Pei, X.; Park, M.; Fakra, S. C.; Liu, Y.-S.; Matheu, R.; Alshmimri, S. A.; Alshehri, S.; Trickett, C. A.; Somorjai, G. A.; Yaghi, O. M. Bioinspired Metal−Organic Framework Catalysts for Selective Methane Oxidation to Methanol. *J. Am. Chem. Soc.* **2018**, *140*, 18208−18216.

(8) Jiang, J.; Gándara, F.; Zhang, Y.-B.; Na, K.; Yaghi, O. M.; Klemperer, W. G. Superacidity in Sulfated Metal−Organic Framework-808. *J. Am. Chem. Soc.* **2014**, *136*, 12844−12847.

(9) Jiang, J.; Yaghi, O. M. Brønsted Acidity in Metal−Organic Frameworks. *Chem. Rev.* **2015**, *115*, 6966−6997.

(10) Logan, M. W.; Langevin, S.; Xia, Z. Y. Reversible Atmospheric Water Harvesting Using Metal-Organic Frameworks. *Sci. Rep.* **2020**, *10*, No. 1492.

(11) Peng, Y.; Huang, H.; Zhang, Y.; Kang, C.; Chen, S.; Song, L.; Liu, D.; Zhong, C. A versatile MOF-based trap for heavy metal ion capture and dispersion. *Nat. Commun.* **2018**, *9*, No. 187.

(12) Li, Z.-Q.; Yang, J.-C.; Sui, K.-W.; Yin, N. Facile synthesis of metal-organic framework MOF-808 for arsenic removal. *Mater. Lett.* **2015**, *160*, 412−414.

(13) Zahn, G.; Zerner, P.; Lippke, J.; Kempf, F. L.; Lilienthal, S.; Schröder, C. A.; Schneider, A. M.; Behrens, P. Insight into the mechanism of modulated syntheses: in situ synchrotron diffraction studies on the formation of Zr-fumarate MOF. *CrystEngComm* **2014**, *16*, 9198−9207.

(14) Wei, R.; Gaggioli, C. A.; Li, G.; Islamoglu, T.; Zhang, Z.; Yu, P.; Farha, O. K.; Cramer, C. J.; Gagliardi, L.; Yang, D.; Gates, B. C. Tuning the Properties of Zr6O8 Nodes in the Metal Organic Framework UiO-66 by Selection of Node-Bound Ligands and Linkers. *Chem. Mater.* **2019**, *31*, 1655−1663.

(15) Alvarez, A. J.; Myerson, A. S. Continuous Plug Flow Crystallization of Pharmaceutical Compounds. *Cryst. Growth Des.* **2010**, *10*, 2219−2228.

(16) Stelzer, T.; Lakerveld, R.; Myerson, A. S. Process Intensification in Continuous Crystallization. In *The Handbook of Continuous Crystallization*; Royal Society of Chemistry, 2020; Chapter 7, pp 266−320.

(17) Chen, D. L.; Gerdts, C. J.; Ismagilov, R. F. Using Microfluidics to Observe the Effect of Mixing on Nucleation of Protein Crystals. *J. Am. Chem. Soc.* **2005**, *127*, 9672−9673.

(18) Millange, F.; El Osta, R.; Medina, M. E.; Walton, R. I. A time-resolved diffraction study of a window of stability in the synthesis of a copper carboxylate metal−organic framework. *CrystEngComm* **2011**, *13*, 103−108.

(19) Ragon, F.; Horcajada, P.; Chevreau, H.; Hwang, Y. K.; Lee, U. H.; Miller, S. R.; Devic, T.; Chang, J.-S.; Serre, C. In Situ Energy-Dispersive X-ray Diffraction for the Synthesis Optimization and Scale-up of the Porous Zirconium Terephthalate UiO-66. *Inorg. Chem.* **2014**, *53*, 2491−2500.

(20) Reinsch, H.; Stock, N. Formation and characterisation of Mn-MIL-100. *CrystEngComm* **2013**, *15*, 544−550.

(21) Cravillon, J.; Schröder, C. A.; Nayuk, R.; Gummel, J.; Huber, K.; Wiebcke, M. Fast Nucleation and Growth of ZIF-8 Nanocrystals Monitored by Time-Resolved In Situ Small-Angle and Wide-Angle X-Ray Scattering. *Angew. Chem., Int. Ed.* **2011**, *50*, 8067−8071.

(22) Stavitski, E.; Goesten, M.; Juan-Alcañiz, J.; Martinez-Joaristi, A.; Serra-Crespo, P.; Petukhov, A. V.; Gascon, J.; Kapteijn, F. Kinetic Control of Metal-Organic Framework Crystallization Investigated by Time-Resolved In Situ X-Ray Scattering. *Angew. Chem., Int. Ed.* **2011**, *50*, 9624−9628.

(23) Liu, Z.; Zhu, J.; Peng, C.; Wakihara, T.; Okubo, T. Continuous flow synthesis of ordered porous materials: from zeolites to metal−organic frameworks and mesoporous silica. *React. Chem. Eng.* **2019**, *4*, 1699−1720.

(24) Bagi, S.; Wright, A. M.; Oppenheim, J.; Dincă, M.; Román-Leshkov, Y. Accelerated Synthesis of a Ni2Cl2(BTDD) Metal−Organic Framework in a Continuous Flow Reactor for Atmospheric Water Capture. *ACS Sustainable Chem. Eng.* **2021**, *9*, 3996−4003.

(25) Ahnfeldt, T.; Stock, N. Synthesis of isoreticular CAU-1 compounds: effects of linker and heating methods on the kinetics of the synthesis. *CrystEngComm* **2012**, *14*, 505−511.

(26) Rowsell, J. L. C.; Yaghi, O. M. Metal−organic frameworks: a new class of porous materials. *Microporous Mesoporous Mater.* **2004**, *73*, 3−14.

(27) Hausdorf, S.; Wagler, J.; Moβig, R.; Mertens, F. O. R. L. Proton and Water Activity-Controlled Structure Formation in Zinc Carboxylate-Based Metal Organic Frameworks. *J. Phys. Chem. A* **2008**, *112*, 7567−7576.

(28) Gualtieri, A. F. Synthesis of sodium zeolites from a natural halloysite. *Phys. Chem. Miner.* **2001**, *28*, 719−728.
(29) Moh, P. Y.; Brenda, M.; Anderson, M. W.; Attfield, M. P. Crystallisation of solvothermally synthesised ZIF-8 investigated at the bulk, single crystal and surface level. *CrystEngComm* **2013**, *15*, No. 9672.
(30) Furukawa, H.; Gándara, F.; Zhang, Y.-B.; Jiang, J.; Queen, W. L.; Hudson, M. R.; Yaghi, O. M. Water Adsorption in Porous Metal−Organic Frameworks and Related Materials. *J. Am. Chem. Soc.* **2014**, *136*, 4369−4381.
(31) McDonald, M. A.; Salami, H.; Harris, P. R.; Lagerman, C. E.; Yang, X.; Bommarius, A. S.; Grover, M. A.; Rousseau, R. W. Reactive crystallization: a review. *React. Chem. Eng.* **2021**, *6*, 364−400.
(32) Forgan, R. S. Modulated self-assembly of metal−organic frameworks. *Chem. Sci.* **2020**, *11*, 4546−4562.
(33) Venna, S. R.; Jasinski, J. B.; Carreon, M. A. Structural Evolution of Zeolitic Imidazolate Framework-8. *J. Am. Chem. Soc.* **2010**, *132*, 18030−18033.
(34) Grand, J.; Awala, H.; Mintova, S. Mechanism of zeolites crystal growth: new findings and open questions. *CrystEngComm* **2016**, *18*, 650−664.
(35) McGinty, J.; Yazdanpanah, N.; Price, C.; ter Horst, J. H.; Sefcik, J. Nucleation and Crystal Growth in Continuous Crystallization. In *The Handbook of Continuous Crystallization*; Royal Society of Chemistry, 2020; Chapter 1, pp 1−50.
(36) Cravillon, J.; Schröder, C. A.; Bux, H.; Rothkirch, A.; Caro, J.; Wiebcke, M. Formate modulated solvothermal synthesis of ZIF-8 investigated using time-resolved in situ X-ray diffraction and scanning electron microscopy. *CrystEngComm* **2012**, *14*, 492−498.
(37) Jiang, M.; Papageorgiou, C. D.; Waetzig, J.; Hardy, A.; Langston, M.; Braatz, R. D. Indirect Ultrasonication in Continuous Slug-Flow Crystallization. *Cryst. Growth Des.* **2015**, *15*, 2486−2492.
(38) Jiang, M.; Zhu, Z.; Jimenez, E.; Papageorgiou, C. D.; Waetzig, J.; Hardy, A.; Langston, M.; Braatz, R. D. Continuous-Flow Tubular Crystallization in Slugs Spontaneously Induced by Hydrodynamics. *Cryst. Growth Des.* **2014**, *14*, 851−860.
(39) Rimez, B.; Debuysschère, R.; Conté, J.; Lecomte-Norrant, E.; Gourdon, C.; Cognet, P.; Scheid, B. Continuous-Flow Tubular Crystallization To Discriminate between Two Competing Crystal Polymorphs. 1. Cooling Crystallization. *Cryst. Growth Des.* **2018**, *18*, 6431−6439.
(40) Neugebauer, P.; Khinast, J. G. Continuous Crystallization of Proteins in a Tubular Plug-Flow Crystallizer. *Cryst. Growth Des.* **2015**, *15*, 1089−1095.
(41) Rubio-Martinez, M.; Hadley, T. D.; Batten, M. P.; Constanti-Carey, K.; Barton, T.; Marley, D.; Mönch, A.; Lim, K.-S.; Hill, M. R. Scalability of Continuous Flow Production of Metal-Organic Frameworks. *ChemSusChem* **2016**, *9*, 938−941.
(42) Vacassy, R.; Lemaître, J.; Hofmann, H.; Gerlings, J. H. Calcium carbonate precipitation using new segmented flow tubular reactor. *AIChE J.* **2000**, *46*, 1241−1252.
(43) Hussain, M. N.; Jordens, J.; John, J. J.; Braeken, L.; Van Gerven, T. Enhancing pharmaceutical crystallization in a flow crystallizer with ultrasound: Anti-solvent crystallization. *Ultrason. Sonochem.* **2019**, *59*, No. 104743.
(44) Pal, S.; Madane, K.; Kulkarni, A. A. Antisolvent based precipitation: Batch, capillary flow reactor and impinging jet reactor. *Chem. Eng. J.* **2019**, *369*, 1161−1171.
(45) Rossi, D.; Jamshidi, R.; Saffari, N.; Kuhn, S.; Gavriilidis, A.; Mazzei, L. Continuous-Flow Sonocrystallization in Droplet-Based Microfluidics. *Cryst. Growth Des.* **2015**, *15*, 5519−5529.
(46) Hirschle, P.; Preiß, T.; Auras, F.; Pick, A.; Völkner, J.; Valdepérez, D.; Witte, G.; Parak, W. J.; Rädler, J. O.; Wuttke, S. Exploration of MOF nanoparticle sizes using various physical characterization methods − is what you measure what you get? *CrystEngComm* **2016**, *18*, 4359−4368.
(47) Song, H.; Chen, D. L.; Ismagilov, R. F. Reactions in Droplets in Microfluidic Channels. *Angew. Chem., Int. Ed.* **2006**, *45*, 7336−7356.
(48) Song, H.; Bringer, M. R.; Tice, J. D.; Gerdts, C. J.; Ismagilov, R. F. Experimental test of scaling of mixing by chaotic advection in droplets moving through microfluidic channels. *Appl. Phys. Lett.* **2003**, *83*, 4664−4666.
(49) Mura, F.; Zaccone, A. Effects of shear flow on phase nucleation and crystallization. *Phys. Rev. E* **2016**, *93*, No. 042803.

https://doi.org/10.1021/acs.cgd.1c00968
Cryst. Growth Des. 2021, 21, 6529−6536